**RESEARCH ARTICLE:**

# Impact of Sintering Temperature of the Mechanical Properties of a $Fe_{20}Cr_{20}Mn_{20}Ni_{20}Ti_{10}Co_5V_5$ Medium Entropy Alloy

Steadyman Chikumba[1] and Veeredhi Vasudeva Rao[2]

**Received:** 12 November 2022 | **Revised:** 04 September 2023 | **Published:** 15 September 2023

**Reviewing Editor:** Dr David Ibrahim, Tshwane University of Technology

## *Abstract*

*Medium entropy alloys (MEAs) are new emerging engineering alloys comprised of four principal elements and characterised by a low enthalpy of mixing and entropies of formation between 1 and 1.5 molar gas constant. They have high strength, wear, and thermal properties. Medium entropy alloyss have generated interest as an alternative material in the last two decades in nuclear, aerospace, and high strength engineering applications. In this research a medium entropy alloy $Fe_{20}Cr_{20}Mn_{20}Ni_{20}Ti_{10}Co_5V_5$ with principal elements Fe, Cr, Mn, and Ni was fabricated using spark plasma sintering. The elemental powder mixture was sintered at temperatures of 870°C, 900°C, and 950°C under 35 bar pressure under an inert argon atmosphere for 45 minutes using an FCT Systeme GmbH spark plasma sintering machine. After sand blasting, the densities of the samples were measured before grinding, polishing, and etching for characterisation. Microstructure analysis was carried out using scanning electron and optical microscopy. Microhardness was measured using a Falcon 507 hardness tester, modulus using an Anton-Paar Nanoindenter, and wear using an Anton-Paar TRB3 Tribometer. The elements form a solid solution with presence of a hard μ phase and soft γ-phase were observed. The hardness of the alloys sintered at 870°C and 900°C were 397 and 424 Vickers respectively. The alloy that sintered at 950°C showed a hardness of 674 Vickers. After annealing the hardness increased to 736 Vickers. The modulus of elasticity and creep resistance increased after heat treatment at 700°C.The other alloys showed a decrease in hardness and other properties after annealing. Unlike in steels, where annealing reduces hardness, in this alloy annealing increased hardness at an appropriate temperature. The alloy $Fe_{20}Cr_{20}Mn_{20}Ni_{20}Ti_{10}Co_5V_5$ MEA exhibited good thermal stability. Further work on the alloy will involve its crystallography and its feasibility for use in elevated temperature energy applications such as in fuel cells, turbines, and wear resistant machine components.*

***Keywords****: spark plasma sintering; mechanical properties; annealing; medium entropy alloy*

## Introduction

Advances in technology used in industrial machinery, equipment in aerospace, transportation energy, and manufacturing has created a demand for materials that can withstand high temperature, wear, temperatures, and loads (Cui *et al*., 2022; Afolabi *et al*., 2019). Modern furnaces, engines, and turbines as well as nuclear reactors and other types of equipment operate under extreme conditions such as elevated temperatures and extreme loading and wear while demanding structural integrity and engineering tolerances (Haase and Barrales-Mora, 2019; Afolabi *et al*., 2019). One such example is in nuclear applications where chemical stability and a resistance to irradiation are also required. To meet these operational demands, new materials are being investigated for elevated temperature applications (Rodriguez *et al*., 2018). There are a number of factors that are considered when selecting constituent elements for manufacturing an alloy in all engineering applications (Horizon technologies Inc., 2018; Zhang *et al*., 2019). These factors include ease of fabrication, corrosion resistance, hardness, tensile strength, impact toughness, and fatigue strength as well as cost (Horizon technologies Inc., 2018; Afolabi *et al*., 2019). Alloy steels and superalloys are common alloys that have been used in the last century (Haase and Barrales-Mora, 2019). New alloys developed recently are high entropy alloys (HEAs) (Miracle and Senkov, 2017) and medium entropy alloys (MEAs) (Murty *et al*., 2019; Cui *et al*., 2022). High entropy alloys and MEAs are

[1]University of South Africa, chikus@unisa.ac.za | https://orcid.org/0000-0003-4908-4076
[2]University of South Africa, vasudvr@unisa.ac.za | https://orcid.org/0000-0003-0759-6954

characterised by unconventional compositions and are not based around a single major component but rather comprise multiple principal alloying elements (Cui *et al*., 2022). The entropies are defined in terms of the molar gas constant R equal to 8.3145 J/Kmol (He *et al*., 2017). High entropy alloys show an entropy of mixing with configuration entropy greater than 1.5R (Afolabi, *et al*., 2019; Cui, *et al*., 2022). Medium entropy alloys have a low enthalpy of mixing and configuration entropy ranging from R and 1.5R (Cui *et al*., 2022). High entropy alloys are equimolar alloys consisting of five or more principal elements, normally transition elements, while medium-entropy alloys can contain up to four principal elements and are non-equiatomic, often containing several equiatomic alloying elements usually transition elements (Zhou *et al*., 2018; Cui *et al*., 2022). These alloys are generating a lot of interest in the energy industry and in other areas with high temperature and strength applications (Haase and Barrales-Mora, 2019), (Afolabi *et al*., 2019). Their attributes include excellent strength, corrosion, toughness, irradiation resistance (Zhao *et al*., 2021), and controllable magnetic properties (Cui *et al*., 2022).

They can produce a diverse and infinite range of properties depending on the relative composition of the constituent elements (Miracle and Senkov, 2017). Cobalt improves alloy strength, especially in terms of creep strength (Zhang *et al*., 2019). The presence of nickel gives an alloy increased strength and toughness and is stabilised by the presence of cobalt (López Ríos *et al*., 2020). Chromium increases corrosion resistance and strength while titanium creates a solid solution strengthened by forming intermetallic compounds (Cui *et al*., 2022). Titanium has a high strength to weight ratio desirable in light weight applications such as in aerospace components (Afolabi *et al*., 2019). Iron is preferred for its low cost and is the basis for many low-cost steels and powder metallurgy components (Horizon technologies Inc., 2018). Vanadium is critical in strength control and retains stiffness and thermal properties in an alloy (Tun *et al*., 2020). The selection of constituent elements for MEAs and HEAs is based on the Hume-Rothery rules for the stability of alloy solid solutions, which is based around the compatibility of three parameters which are: (a) the atomic size misfit between solvent and solute, $\delta$, which tends not to exceed ≈15% for stable solid solutions; (b) the electronegativity difference between two alloy components, $\delta x$ , which tends to be larger in alloys that contain intermetallic compounds; and (c) the electron concentration, which is the valence electron concentration (Murty *et al*., 2019).

Fabrication methods for these alloys include mechanical alloying and powder metallurgy among other techniques (López Ríos *et al*., 2020; Miracle and Senkov, 2017). Spark plasma sintering is a powder metallurgy technique involving the simultaneous compaction and sintering of a powder mixture in a graphite die using a pulsed current as a heating medium (Sharma *et al*., 2019). During the sintering process, punches apply pressure to compact the powder mixture through hydraulic or pneumatic actuators. The current and voltage are also controlled to regulate the heating and cooling process during sintering (Total Materia, 2016; Ogunbiyi *et al*., 2020). The arrangement of a spark plasma sintering machine and its control equipment is shown in Figure 1.

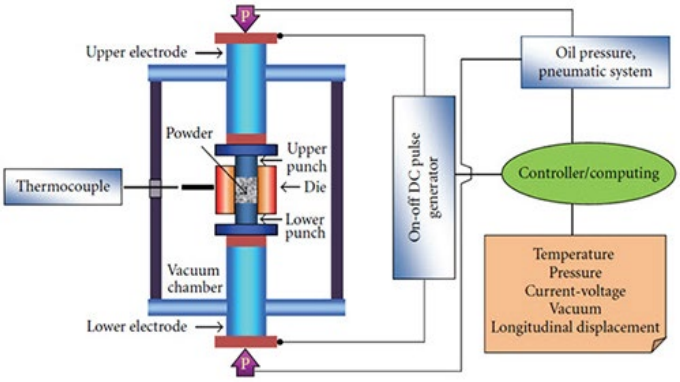


**Figure 1**: Arrangement of spark plasma sintering equipment (Total Materia, 2016)

For the process to reach the sintering temperature the holding time, ramp rate, pulse duration, and pulse current and voltage are set and automatically controlled (Total Materia, 2016). Resultantly the DC pulse discharge is able to generate spark plasma, spark impact pressure, joule heating, and an electrical field diffusion effect (Total Materia, 2016; Afolabi *et al*., 2019; Ogunbiyi *et al*., 2020). Punches are used to compact the mixture and also act as an anode (Total Materia, 2016). Sintering results in the fabrication of near net shape alloy and ceramics which are part of high densification (Afolabi *et al*., 2019). A typical sintering temperature range is between 30 percent to 60 percent of the melting temperature of the lowest melting constituent element or material in the powder mixture. This can result in a fast sintering rate without causing too much grain growth in crystalline materials (Sharma *et*

*al*., 2019). The main advantage of SPS is low power consumption, quick processing times, and that minimal phase transformation occurs during the brief sintering period (Althahban *et al*., 2022).

Annealing involves the heating and slow cooling of an alloy so as to alter the physical, and sometimes chemical, properties of a material. It also increases its ductility and softness and makes it more workable for subsequent processing steps, such as forging or drawing in component manufacturing (Onwuamaeze *et al*., 2018). During annealing, the material is heated to a point above its recrystallisation temperature, maintained at that temperature, and then cooled to room temperature (Zhao *et al*., 2021; Kang *et al*., 2021). In the process, atoms migrate in the crystal lattice and the number of dislocations decreases, leading to a change in ductility, softening the metal or alloy (Kang *et al*., 2021; Materials Today, 2022). Annealing in most alloys and metals improves machinability, refines the grain size due to phase recrystallisation, and increases the ductility of the metal (Onwuamaeze *et al*., 2018). In addition to preparing the material for subsequent treatment, annealing can also be used to modify electrical and magnetic properties, relieve internal stresses, remove gases, and produce a definite microstructure (Onwuamaeze *et al*., 2018; Zhao *et al*., 2021).

Researchers have observed an increase in hardness and other mechanical properties after annealing sintered alloys (Cui *et al*., 2022; Guruvidyathri *et al*., 2017). The effect of annealing effect also observed in medium entropy alloys (MEAs) which are composed of the γ phase of the FCC structure μ phase microstructures. Formation of the μ phase, which could result in the precipitation strengthening, the inhibition of grain growth, as well as recrystallisation by the Zener pinning effect which is stress-induced ordering of solute atoms in a solid solution (Zhang *et al*., 2020). A challenge encountered in medium entropy alloy (MEA) research is obtaining single-phase solid solutions (Murty *et al*., 2019), but often one encounters situations where topologically close-packed (TCP) phases are present in the microstructures (Guruvidyathri *et al*., 2017). They are detrimental to the overall high-temperature performance of alloys and in the case of superalloys because they are not only brittle but also deplete the Ni-rich matrix of potent solid-solution strengthening elements (Bezold *et al*., 2022). This precipitation of new carbides and the μ phase creates a depleted zone of γ-matrix strengthening elements, reducing γ-strength and increasing the proportions of γ ' -formers within this zone (Jana *et al*., 2018). Research in alloys, with Cr, W, and Mo for example, has shown that C demonstrates the presence of needle-like precipitates in the interdendritic region and connected to some carbide (Jana *et al*., 2018). These precipitates are assumed to be TCP μ phase. When they decompose, they release C into the matrix. The released carbon then subsequently reacts with either Cr to form M23 C6 to form MC. This reaction leads to increase in embrittlement (López Ríos *et al*., 2020). Topologically close-packed phase formation is stronger in the material with the coarser dendrite structure due to less effective diffusional flow and homogenisation during heat treatment due to smaller concentration gradients and larger distances (Bezold *et al*., 2022). Many sintered alloys are reported to show no TCP phase after synthesis, which may end up having these phases during elevated temperature service (Guruvidyathri *et al*., 2017).

## Materials and Methods

In this research five medium entropy alloy samples were fabricated through spark plasma sintering at different temperatures. The sintered alloy was fabricated from seven metallic elements. The metal powders were supplied by Sigma-Aldrich company and Table 1 shows their compositional specifications:

**Table 1**: Composition and powder grain size for powders

| Element | Particle size | Purity% | Element | Particle size | Purity% |
|---|---|---|---|---|---|
| Ti | <45micron | 99.8 | Cr | -100mesh | 99.5 |
| Fe | <45micron | 99.9 | Ni | <150micron | 99.99 |
| V | 325 mesh | 99.5 | Co | <45micron | 99.99 |
| Mn | 325 mesh | 99.5 | | | |

The elemental metal powders were mixed in a tubular mixer and sintered in graphite dies to make samples with a 20 mm diameter and 10 mm thickness. The first step involved in the procedure involved the calculation of the material quantities in the form of powders required for sintering. The calculation of the volume (V) of the die cavity after sintering is given as 3.142 $cm^3$. The mass of the powder mixture is the volume of the fully dense body after sintering is multiplied by $\rho_m$ of the density of mixture. If $W_i$ and $\rho_i$ are the weight percentage and the densities of constituent element powder in the sintered alloy powder thus:

$$\frac{1}{\rho_m} = \frac{\%W_i}{\rho_i} + \frac{\%W_2}{\rho_2} + \cdots + \frac{\%W_n}{\rho_n} \quad (1)$$

Table 2 shows the melting point, density, and weight percentage of constituents in the alloy for calculating elemental masses and sintering temperature. The total mass of the sintered powder is the product of the die cavity volume 3.142 $cm^3$ multiplied by the theoretical density of the mixture 7.19g/$cm^3$ and then multiplied by the weight percentage in the alloy. By considering elemental composition in Table 2 and substituting into equation 1 the density of the mixture, $\rho_m$ is equal to 7.19 g/$cm^3$. The calculated masses of the elemental powders mixed for sintering are also shown in Table 2.

**Table 2**: Density, melting point, % alloy elemental weight and individual elemental powder mass

| Element | Fe | Cr | Mn | Ni | Ti | Co | V |
|---|---|---|---|---|---|---|---|
| Melting point (°C) | 1538 | 1860 | 1473 | 1453 | 1 668 | 1492 | 1910 |
| Density (ρ) g/$cm^3$ | 7.9 | 7.15 | 7.21 | 8.9 | 4.5 | 8.9 | 6.1 |
| % Weight | 20 | 20 | 20 | 20 | 10 | 5 | 5 |
| Mass (g) | 4,52 | 4,52 | 4,52 | 4,52 | 2.26 | 1.13 | 1.13 |

The powders were weighed and mixed in a Willy A Bachofen (WAB) AG Tubular mixer manufactured in Germany with specifications 230 V, 50 Hz 0.18 kN for 16 hours. The sintering process was done in an FCT Systeme spark plasma-sintering machine manufactured in Germany, with specifications which include a H-HP D 25 hybrid heated FAST/SPS furnace, a pressing force of 250 kN, a heating power FAST of 64 kW, a heating power induction of 80 kW, and a maximum component diameter of 100 mm. The minimum sintering temperature of 60 percent of the melting temperature of the lowest melting constituent element or material in the powder mixture was used (Sharma *et al*., 2019). In Table 2 the melting points of the constituent elements are shown. For the alloy, the minimum sintering temperature is calculated from 60 percent of what is considered the melting point of Mn (1453°C), which is 871°C. A higher temperature promotes higher densification. For this work, samples were sintered at 870°C, 900°C, and 950°C. The sintering parameters are in Table 3.

**Table 3**: Sintering Parameters for the experiment

| | | | |
|---|---|---|---|
| Sintering pressure | 35 bars | Holding time | 10 mins |
| Sintering temperature | 870°C, 900°C and 950°C | Heating rate | 100°C/min |
| Sintering time | 45 mins | | |

After sintering, the samples were prepared for characterisation through cutting, grinding, and polishing using with Struers Laboforce 100 polisher manufactured in Denmark. Aka Piatto 220 was used as a grinding and polishing agent. Etching of the polished samples in three percent Nital solution was conducted for 60 seconds at room temperature before microstructural analysis.

### *Microstructural analysis*

The microstructure was studied using an optical microscope incorporated in the microhardness tester. The microstructure was observed under the optical microscope with a magnification of ×100. Micro-hardness tests were conducted on the polished samples using an Innovatest Falcon 507 micro-instrument. A load of HV/20 was used with a dwell time of ten seconds. Hardness measurement is a measure of resistance to deformation of a material. In principle, hardness is quantified as the ratio of the applied indenting load (P) to the indentation area (A), mathematically shown in equation 2 as P.

$$H = \frac{P}{A} \tag{2}$$

A is the projected contact area between the indenter and the specimen.

### *Nanoindentation hardness testing*

Instrumented nanoindentation was employed to determine the nanohardness and derive other mechanical properties such as the modulus of elasticity, percentage elastic work, and creep rate at room temperature. During nanoindentation measurement and analysis, the Oliver and Pharr method was used to determine the hardness and elastic modulus (Helmut Fischer Technology Inc, 2022; Fischer-Cripps, 2010). A Load-depth curve can be drawn together with a power law curve to the unload data points which is then extrapolated to the fully unload final indentation depth. The slope S at the maximum load data point is critical to calculate the elastic modulus (Nemecek, 2009; Nano Science Instruments, 2022). When the modulus of elasticity takes into account the sample and indentor modulus of elasticity it is called the reduced elastic modulus $E_r$.

$$E_r = \frac{S}{2}\left(\frac{P_i}{A_i}\right)^{1/2} \quad (3)$$

For the nanoindentation experiment, a projected contact area A for a Berkovich indenter was used ($A = 35.36(h_r+h_0)^2$), where $h_r$ is the plastic depth under loading (m), $h_0$ the tip indenter defect ($10^{-9}$ m), and P the applied load (N) (Tankiewicz, 2018).

Using the Oliver and Pharr method to determine the hardness and elastic modulus (Oliver and Pharr, 1992; Zorzi and Perottoni, 2013), the composite modulus E*, modulus of the specimen can be extracted from the effective modulus using.

$$\frac{1}{E_r} = \frac{1-v^2}{E^*} + \frac{1-v_i^2}{E_i} \quad (4)$$

Where E* and $E_i$ is the moduli of the specimen material and indenter, $\nu$ and $\nu_i$ are Poisson's ratios for the specimen and the indenter, respectively. The modulus of elasticity of the diamond Berkovich indenter is 1140 GPa (Kushch *et al*., 2007). During the nanoindentation process there is elastic energy ($W_{elast}$) and plastic energy ($W_{plast}$). Elastic energy is released during the unloading phase of the experiment (Sun *et al*., 2018; Fischer-Cripps, 2010). However, the plastic energy is permanently stored in the sample material (Sun *et al*., 2018). According to the ISO14577 indentation work ratio, "ηIT" is a ratio of the indentation work by elastic deformation "Welast" to the mechanical work caused during the indentation process "Wtotal" (ISO14577: 2002, 2002). Indentation creep (CIT) is another important property observed during nanoindentation which shows the change in indentation depth at a constant load on the sample material indenter denoted by the expression:

$$CIT = \frac{h_1-h_2}{h_1} \times 100\% \quad (5)$$

An Anton Paar NHT$^3$ nano indenter manufactured in Austria was used for instrumented nanoindentation testing. A Berkovich indenter was used while a Poisson's ratio of 0.3 was assumed since the material is metallic (Nemecek, 2009). The following parameters on the instrument were used: maximum linear load of 400.00 mN, loading/unloading rate of 600.00 mN/min, data acquisition rate of 400.0 Hz, approach distance of 3000 nm, approach speed of 200000.001 nm/min, and a retract speed of 2000 nm/min. The pause time was 20.0 seconds. Using the Oliver and Pharr method, the indentation nanohardness, nanohardness, and elastic modulus were evaluated (Fischer-Cripps, 2010). The percentage elastic work and indentation creep at room temperature were also obtained from the test.

### *Annealing*

The impact of annealing on the alloy sintered at 950$^o$C was studied by heating the samples in a furnace at different temperatures before allowing them to cool in the air. After this annealing process they were characterised by studying their microstructures and measuring their microhardness. The aim of the study was to determine how annealing temperature affects the sample microhardness and related properties such as the yield strength. The temperature range of the study was 600$^o$C to 1000$^o$C. The annealing process was conducted in a heat treatment Muffle Furnace: TP Series Model 15/12/B510 supplied by Labfriend South Africa. The duration of each heat treatment cycle was five hours. Each heating time was 30 minutes and there was a holding time of four and a half hours. After heating at a selected temperature, each sample was retrieved from the furnace and allowed to cool in open air. The process was meant to mimic how machine components are exposed to heat in operation and cooled when a machine is switched off.

### *Wear measurement*

Wear measurement was carried out using a ball on disk method (Xiao *et al*., 2020). The coefficient of friction (μ) is the resistance occurring when the material surface moves over another in relative motion either rolling or sliding (Burwell and Strang, 1952; Kucharski and Mróz, 2011). Its value must lie between 0.1 and 1 for materials in sliding air and is calculated by the expression:

$$\mu = \frac{f_t}{f_n} \quad (6)$$

The ball wear rate is expressed by:

$$W_{ball} = \frac{V_{ball}}{f_n l} \quad (7)$$

The disk wear rate is expressed by:

$$W_{disk} = \frac{V_{disk}}{f_n l} \quad (8)$$

The variants $f_n$, $f_t$, and $l$ are the normal load, tangential force, and distance travelled, respectively (Kucharski and Mróz, 2011; Xiao *et al*., 2020).

The wear properties were measured by a TRB$^3$ Tribometer, Version 8.1.8 instrument manufactured by Anton-Paar in Austria. Wear tests involved the use of a pin on disc. The process involves applying a constant normal load of 15N in the contact while rotating the disc at a constant speed. The measured sample weight loss is stored to calculate the wear rate. The parameters for the test specifications included an AM Static partner of 6.00 mm diameter, indenter geometry: ball sample. Lab conditions consisted of a temperature of 26.64 °C with a target temperature of 24.00°C, an atmospheric pressure of 1014 mbars, and humidity at 40.33 percent. The linear speed of the test was set at 0.06 cm/s and the acquisition rate at 15.0 Hz.

## Results and Discussion

The alloy $Fe_{20}Cr_{20}Mn_{20}Ni_{20}Ti_{10}Co_5V_5$ alloy was successfully fabricated using the Spark plasma sintering technique. This is a fast end economic method of producing small quantities of near net shape parts. In this is study it was proved that the important mechanical properties of microhardness and yield strength increased with increased sintering temperatures. There was an increase in the sample modulus of elasticity and hardness of the alloy. Higher sintering temperatures improves the diffusion of the atoms in the solute structure and is governed by relative atomic radii, electrovalence', and a mutual affinity for constituent element. This is supported by the Hume-Rothery rules (Cui *et al*., 2022; *Tun et al*., 2020). A temperature of 950$^o$C achieved a higher density of the alloy compared to 900$^o$C and 870$^o$C. The alloy sintered at higher temperatures achieved a higher microhardness, yield strength, and modulus of elasticity. This effect of sintering temperature on sample properties is supported by literature (Sharma *et al*., 2019; Ogunbiyi *et al*., 2020)

The sample was measured using the Archimedes principle. The relative density was compared with the theoretical alloy sample. Five measurements were taken for each sample and the average density was calculated. The relative density was calculated using the measured average density divided by the theoretical density 7.19 g/cm$^3$. The sintering process was able to achieve a high level of densification. For the samples sintered at different temperatures the results are tabulated in Table 4.

**Table 4**: Relative densities for samples sintered at different temperatures.

| | | Mean density(g/cm3) | Relative density |
|---|---|---|---|
| Sample | 870 oC | 7.0876 | 98.09% |
| | 900 oC | 7.0876 | 98.56% |
| | 950 oC | 7.137 | 99.22% |

The highest densification was achieved by the sintering temperatures of 950$^o$C. This sample is tested for further characterisation since it has the highest consolidation from the sintering.

### *Microstructural analysis and microhardness before heat treatment*

Micrographic analysis was conducted to determine the microstructure of the alloy the samples were polished and etched using a three percent Nital solution and viewed under the Innovatest Falcon 507 optical microscope manufactured in the Netherlands. Figure 1(a) shows the microstructure before and Figure 1(b) shows the microstructure after heat treatment in a furnace at 700$^o$C for five hours. The microstructures of $Fe_{20}Cr_{20}Mn_{20}Ni_{20}Ti_{10}Co_5V_5$ sintered at 700$^o$C were studied at ×100 magnification and are shown Figure 2. The micrograph shows the changes in the grain size and microstructural transformation at this temperature.

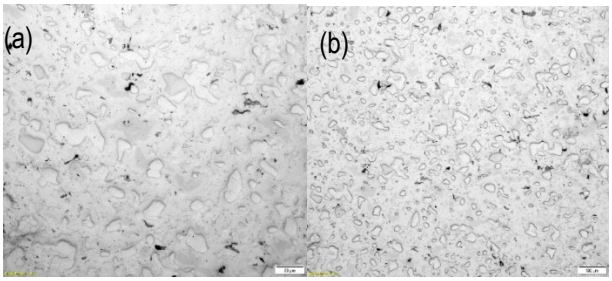


**Figure 2**: Micrography of $Fe_{20}Cr_{20}Mn_{20}Ni_{20}Ti_{10}Co_5V_5$ samples sintered at 950°C (a) before heat treatment (b)after annealing at 700°C

Sample (a) showed more grain refinement after heat treatment. Carbides also decreased in concentration and occurrence within the microstructure; there was increase in the proportion of the μ-phase. The samples were studied using an Oxford Instruments Scanning Electron Microscope to establish the composition. Figure 3 and Figure 4 show the compositional analysis and elemental distribution of the alloy sintered at 950°C, respectively. Although the mixture of the powder had a 20 percent composition of the major elements, the resultant alloy had a composition of less than 20 percent due to relative solubilities, losses, and reactions with oxygen and carbon. Mn and Cr tend to form oxides MnO and CrO in the alloy. The constituent elements also form intermetallic compounds that segregate to grain boundaries. Examples of these nonstoichiometric intermetallic compounds are NiTi, FeTi, and CoTi which have higher hardness than stoichiometric ones and are brittle at room temperature (Chu *et al*., 2019).

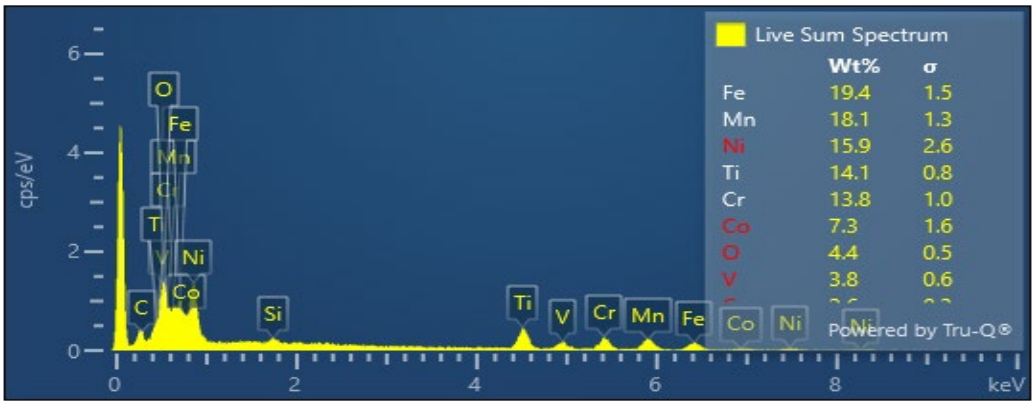


**Figure 3**: Elemental composition of alloy sintered at 950°C

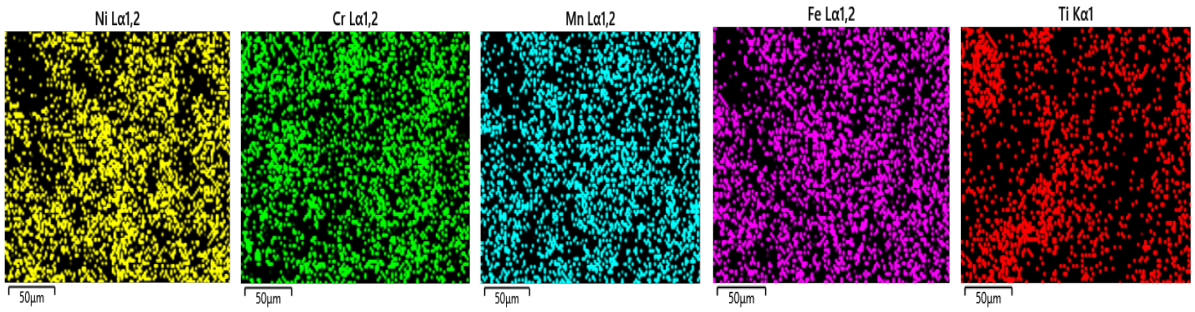


**Figure 4**: Elemental map of constituent elements for alloy sintered at 950°C

The elemental map shows an even distribution of the five principal elements Fe, Mn, Ni, Ti, and Cr, which form the matrix phase. Cobalt and vanadium are absorbed as solute atoms in the microstructure structure of the alloys. Cobalt and vanadium are known for being straighteners, providing both ductility and creep strength in the alloy (Haase and Barrales-Mora, 2019; Zhang *et al*., 2020). Two phases were observed in Figure 2 (a) and (b) showing μ phase, which is light coloured in ferritic phase, and γ-phase which is dark phase. There are also black dispersed carbides originating from the die and punch's graphite material used for sintering. There is also material loss during the sintering process.

### *Microhardness, yield stress*

Microhardness measurements over the sample surface and the average microhardness are shown in Table 5. The yield stress of the alloys is calculated using the Tabor equation σ =H/3, where H is the microhardness (Tankiewicz, 2018).

**Table 5**: Microhardness (Vickers) values of the alloys before heat treatment

| Sample | Hardness 1 | Hardness 2 | Hardness 3 | Hardness 4 | Hardness 5 | Mean hardness |
|---|---|---|---|---|---|---|
| **950°C** | 652 | 660 | 663 | 691 | 705 | 674 |
| **900°C** | 430 | 430 | 434 | 409 | 415 | 424 |
| **870°C** | 404 | 399 | 373 | 373 | 436 | 397 |

Alloys sintered at higher temperatures resulted in higher consolidation of the powder, densification, and higher hardness. The sample sintered at 950°C has an average hardness of 674 Vickers, which is higher than the alloys sintered at 870°C and 900°C. Among the alloys sintered, it is the best alloy in terms of density and microhardness. Further studies were pursued on this alloy. Table 6 contains the measured microhardness values of the alloy sintered at 950°C after it was heat treated at different temperatures. The yield stress is calculated from the Tabor equation (Tankiewicz, 2018).

**Table 6**: Vickers microhardness and yield stress values of the alloy sintered at 950°C after heat treatment at different temperatures

| Sintering temperature | Annealing temperature | 1 | 2 | 3 | 4 | 5 | 6 | Average Hardness (H) Vickers | Yield stress ($\sigma_y$) MPa |
|---|---|---|---|---|---|---|---|---|---|
| 950°C | 600°C | 445 | 517 | 567 | 533 | 534 | 518 | 519 | 173.0 |
| | 700°C | 757 | 729 | 733 | 741 | 721 | 736 | 736 | 245.3 |
| | 800°C | 625 | 690 | 659 | 725 | 671 | 630 | 667 | 222.3 |
| | 900°C | 580 | 532 | 517 | 498 | 661 | 585 | 562 | 187.3 |
| | 1000°C | 408 | 352 | 388 | 387 | 379 | 397 | 321 | 106.9 |

Alloys sintered at higher temperatures resulted in higher consolidation of the powder, densification, and higher hardness. For samples sintered at 950°C there was an average hardness of 674 Vickers. Shear strength is its resistance to forces acting in a direction parallel to a surface or to a planar cross section of a body (Varvenne *et al*., 2016). Shear stress is estimated using:

$$\tau_y(T, \dot{\varepsilon}) = 3.06\sigma_y(T, \dot{\varepsilon}) \quad (9)$$

$\dot{\varepsilon}$ is a reference strain rate connected to dislocation density equal to $10^{-3}s^{-1}$ for high entropy alloys (Bracq *et al*., 2019; Varvenne *et al*., 2016). The calculated shear strength for the alloys sintered at different temperatures are in Table 7.

**Table 7**: Yield stress and shear stress for alloys sintered at different temperatures

| Sintering temperature (°C) | Vickers Hardness *H* | Yield strength $\sigma_y$(MPa) | Shear Yield stress $\tau_y$(MPa) |
|---|---|---|---|
| **950** | 674 | 224.6 | 687.3 |
| **900** | 424 | 141.3 | 432.4 |
| **870** | 397 | 132.3 | 404.8 |

For the alloy sintered at 950°C, before annealing σ = 224.7MPa. There is an increase in strength of the alloy sintered at a higher temperature.

### *Modulus of elasticity*

The alloy sintered at 950°C was tested using nanoindentation to derive the Youngs modulus and other properties. The sintered and annealed samples were tested using a set of ten indentations on the polished sample surface. The sample indentation hardness (HIT), modulus of elasticity E*, and reduced modulus of elasticity Er values for the $Fe_{20}Cr_{20}Mn_{20}Ni_{20}Ti_{10}Co_5V_5$ sintered at 950°C before the annealing heat treatment are shown in Table 8 and 9, respectively. There is an increase in the Vickers indentation nano hardness of the sample after heat treatment. This is attributed to the change in the microstructure and the separate phases. After sintering, the main phase is

Face Centred Cubic (FCC) in a medium entropy alloy which is relatively soft (Miracle and Senkov, 2017). However, after heating to higher temperatures, intermetallic and carbide phases develop (Bracq *et al*., 2019). Similarly, the different moduli for the sample increases since there is a direct correlation between the modulus of elasticity and indentation hardness (Helmut Fischer Technology Inc, 2022; Fischer-Cripps, 2010).

**Table 8**: Nanoindentation results before heat treatment for $Fe_{20}Cr_{20}Mn_{20}Ni_{20}Ti_{10}Co_5V_5$ alloy sintered at 950°C

| Temperature (°C) | Indent | HIT(MPa) | EIT (GPa) | E* (GPa) | Er (GPa) | CIT (%) | nIT (%) |
|---|---|---|---|---|---|---|---|
| No annealing | 1 | 26 038 | 197.65 | 217.2 | 182.61 | -4.75 | 64.45 |
| | 2 | 96 864 | 581.47 | 638.98 | 410.32 | -0.65 | 87.25 |
| | 3 | 12 770 | 149.84 | 164.66 | 143.98 | 0.45 | 40.42 |
| | 4 | 78 189 | 502.15 | 551.81 | 372.53 | 1.81 | 75.65 |
| | 5 | 14 985 | 171.93 | 188.93 | 162.2 | 1.38 | 42.20 |
| | 6 | 60 258 | 449.54 | 494 | 345.25 | 2.34 | 73.95 |
| | 7 | 31 468 | 275.17 | 302.39 | 239.28 | 1.99 | 54.73 |
| | 8 | 67 734 | 486.63 | 534.75 | 364.68 | 2.43 | 76.67 |
| | 9 | 28 176 | 261.17 | 287 | 229.55 | 1.90 | 58.08 |
| | 10 | 52 479 | 413.87 | 454.81 | 325.64 | 2.30 | 74.71 |
| Average | | 46 896.1 | 348.94 | 383.45 | 259.36 | 3.49 | 64.8 |

**Table 9**: Nanoindentation results after annealing at 700°C for $Fe_{20}Cr_{20}Mn_{20}Ni_{20}Ti_{10}Co_5V_5$ alloy sintered at 950°C

| Temperature (°C) | Indent | HIT (MPa) | EIT (GPa) | E* (GPa) | Er (GPa) | CIT (%) | nIT (%) |
|---|---|---|---|---|---|---|---|
| 700 | 1 | 10 373 | 186.31 | 204.73 | 173.72 | -0.42 | 40.48 |
| | 2 | 1.2829E005 | 1578.2 | 1734.3 | 690.26 | 2.59 | 76.10 |
| | 3 | 11 504 | 194.71 | 213.96 | 180.31 | 1.34 | 35.47 |
| | 4 | 61 632 | 665.5 | 731.32 | 446.53 | 2.90 | 67.08 |
| | 5 | 16 435 | 233.47 | 256.56 | 209.65 | 1.84 | 38.41 |
| | 6 | 73 579 | 665.19 | 730.98 | 446.4 | 2.23 | 73.80 |
| | 7 | 20 849 | 255.77 | 281.07 | 225.73 | 1.77 | 44.92 |
| | 8 | 83 306 | 690.26 | 758.53 | 456.52 | 2.40 | 75.86 |
| | 9 | 32 338 | 334.62 | 367.72 | 278.43 | 2.18 | 53.44 |
| | 10 | 95 682 | 739.92 | 813.10 | 475.74 | 1.71 | 78.51 |
| Average | | | 554.40 | 609.22 | 358.33 | 1.8 | 65.15 |

Due to the increase in the material hardness after the annealing process, the room temperature creep (CIT) decreases. At a constant load the tendency to change indentation depth is, therefore, reduced. The percentage of elastic work is an indicator of the reduced amount of plastic deformation in the sample. Softer materials suffer less elastic work compared to plastic work during the indentation process. This indicates that the sample annealed at 700°C gains higher material hardness and strength than the one that was not annealed.

### *Wear results*

The three samples sintered at 870°C, 900°C, and 950°C were tested for wear at a load of 15N and results are in Table 10. The wear track size, the wear rate, the minimum maximum, and mean recorded coefficient of friction and their standard deviations during the test are reported.

| Alloy | Wear track (µm) | Wear rate [mm³/N/m] | Minimum µ | Maximum µ | Mean µ | Std deviation σ |
|---|---|---|---|---|---|---|
| 950oC | 236.0 | 5.243E-006 | -0.007 | 0.182 | 0.104 | 0.054 |
| 900°C | 8616.1 | 0.0001914 | -0.190 | 0.568 | 0.326 | 0.107 |
| 870°C | 30040.3 | 0.0006673 | 0.000 | 0.676 | 0.445 | 0.111 |

**Table 10**: Wear test results for Fe20Cr20Mn20Ni20Ti10Co5V5 alloys sintered at 950oC, 900oC and 870oC

Table 11 indicates a comparison of wear test results for tests conducted for the $Fe_{20}Cr_{20}Mn_{20}Ni_{20}Ti_{10}Co_5V_5$ sintered at 950°C for its as-sintered state and after it was annealed at 700°C for five hours and air cooled. The wear track size before annealing was 236.0 µm² while after annealing it was 26.6 µm². Similarly, there was a reduction in the wear rate from 5.243E-006 to 5.908E-007 mm³/N/m after annealing. The wear curves for the two samples are shown in Figure 5.

**Table 11**: Wear characteristics before and after annealing

| | Wear characteristics before annealing | Wear characteristics after annealing |
|---|---|---|
| Worn Track Section: [µm²] | 236.0 | 26.6 |
| Sample Wear Rate: [mm³/N/m] | 5.243E-006 | 5.908E-007 |
| Coefficient of friction mean | 0.104 | 0.464 |
| Standard deviation | 0.054 | 0.123 |

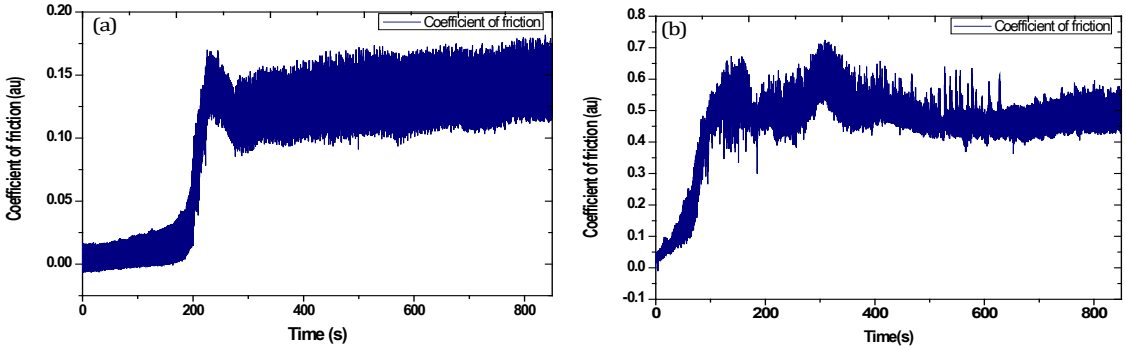


**Figure 5**: Wear profile (a) before annealing (b) after annealing

An increase in the coefficient of friction is recorded after annealing at 700°C. This phenomenon can be attributed to a phenomenon of nanolayering (Yang *et al*., 2021; Ghasemi *et al*., 2017). In the alloy that is not heat treated, there is formation of self-organised, nanolayered structures which result in a significant reduction in the coefficient of friction and wear rate. This tendency, however, is diminished after the change in microstructure following the annealing process, thus, the coefficient of friction is observed to increase (Yang *et al*., 2021). While most medium entropy alloys hold an FCC structure, meaning they are soft, intermetallic phases have a very high hardness and modulus of elasticity, as shown in Tables 8 and 9 (Miracle and Senkov, 2017). Wear rate decrease in the alloy sintered at a higher temperature, corresponding to a higher hardness and yield strength achieved. Similarly, the friction coefficient is reduced due to the reduction in adhesion tendencies of the sample during wear testing. The main mechanism of wear in the harder alloy can be attributed to abrasive wear. In the softer one sintered at lower temperatures it is mainly due to the adhesion weld and shear of the softer surface. This is supported by literature (Burwell and Strang, 1952; Chusong *et al*., 2020; SKF Evolution, 2019).

### *Microstructure and nanoindentation of $Fe_{20}Cr_{20}Mn_{20}Ni_{20}Ti_{10}Co_5V_5$ MEA*

From the nano indentation results in Table 8, there is a wide variation in the indentation hardness (HIT). A value of 12 770 MPa is the lowest while the highest is 96 864 MPa, with a wide variation in between. The primary phase of the $Fe_{20}Cr_{20}Mn_{20}Ni_{20}Ti_{10}Co_5V_5$ is an FCC solid solution which corresponds to the lowest indentation hardness. According to literature, the entropy of mixing in medium and high entropy alloys is high due to their compositions and in theory should favour the formation of a simple solid solution (Tun *et al.*, 2020). There is a tendency towards the formation of simple solid solutions which seeks to suppress that of undesirable complex an intermetallic structures (Cui *et al.*, 2022); in practice it is a challenge to obtain a single-phase solid solution (Murty *et al*., 2019). There are other secondary phases that also form in medium entropy alloys due to constituent elements' relative solubilities, intermetallic compounds, and impurities, such as carbides (Zhou *et al*., 2018; Cui *et al*., 2022; Miracle and Senkov, 2017). These other phases from the study showed indentation hardness values ranging form 52 479 MPa.

In addition to body centred (BCC) and face centred (FCC) structures, which theoretically should result from medium entropy alloys, topologically close-packed (TCP) phases are present in the microstructures (Guruvidyathri *et al.,* 2017). Topologically close-packed phases are intermetallic phases that are considered undesirable (Guruvidyathri *et al.,* 2017). Topologically close-packed phases reduce the high-temperature performance by causing embrittlement and deplete the Ni-rich matrix of solid-solution strengthening elements in the microstructure (Guruvidyathri *et al*., 2017; Bezold *et al*., 2022). The presence of carbides in the composition depletes strengthening elements such as chromium within certain areas (Jana *et al*., 2018; Bezold *et al*., 2022). There are cases where the TCP structure is desirable. The µ phase is in the form of precipitates are assumed to be TCP

associated with high hardness (Schröders *et al*., 2018). The presence of carbon in the microstructure precipitates in the form of softer primary (MC) carbides of elements, such as titanium in the form of TiC or other hard secondary ($M_{23}C_6$) carbides with elements like chromium and cobalt. The primary carbides are large and stable mono carbides, especially the TiC carbide (Haase and Barrales-Mora, 2019). It has been observed that there is an increase and local enrichment of Co, Cr, Mn, and V near boundaries of MC carbides (Haase and Barrales-Mora, 2019; Jana *et al*., 2018). Although alloys containing Co and Cr after sintering showed no presence of TCP phases, these phases were only observed after the alloys were exposed to high temperatures (Guruvidyathri *et al*., 2017). The existence of intermetallic phases and carbides were supported by a nanoindentation experiment. The corresponding Vickers nanohardness value HVIT can be estimated by dividing the HIT value by a factor of 10.58 (Oliver and Pharr, 2004). The indentation nanohardness evaluates the phases present in the sample while the microhardness indicates the general hardness.

***Annealing and impact on mechanical properties***

Annealing the alloys at different temperatures affected mechanical properties. A study of the alloy sintered at 950°C showed an increase in the hardness upon annealing at 700°C followed by a decline thereafter; other researchers have observed the same phenomenon after annealing sintered alloys. Studies on the annealing of sintered copper alloys also reported the same results; annealing occurs at 450-650K. Heating the alloys above this temperature range leads to hardening and mechanism for this behaviour is called annealing effect (Gohar *et al*., 2018). It has been observed that the strength properties of substitutional solids are increased by annealing up to recrystallisation temperature due to solute segregation to dislocations. The annealing hardening effect is more expressive in ternary than binary alloy systems (Gohar *et al*., 2018). The solute segregation to dislocations and the resulting binding force is the primary cause of anneal hardening (Gohar *et al*., 2018). The annealing effect depends on recrystallisation temperature and the presence of nickel has been found to increase recrystallisation temperatures (Bezold *et al*., 2022). Studies have revealed that the annealing effect is often observed in medium entropy alloys (MEAs) which are mostly composed of γ phase and μ phase microstructures. The μ phase is associated with high hardness (Zhang *et al*., 2020). An increase in the proportion of μ phase microstructures causes precipitation hardening which leads to an inhibition of grain growth and recrystallisation (Zhang *et al*., 2020). Precipitation hardening is a common phenomenon in medium entropy alloys since they have many constituent elements and are prone to crystalline defects (Murty *et al*., 2019).

## Conclusion

The spark plasma sintering technique successfully fabricates the Fe20Cr20Mn20Ni20Ti10Co5V5 alloy. A sintering temperature of 870°C is chosen as the least feasible sintering temperature at a pressure of 35 bars. Sintering further samples at 900°C and 950°C yielded samples with microhardness values of 397, 424 and 674 Vickers and relative densities of 98.08, 98.56, and 99.22 percent, respectively. A higher sintering temperature also promotes both densification and mechanical properties such as yield strength and modulus of elasticity. The primary crystal structure in the high entropy alloy is FCC, with secondary phases due to intermetallic compounds and carbides in the form of μ, γ' phases. Some of the intermetallic phases of Cr and Co segregate to grain boundaries. The indentation nanohardness (HIT) ranges from 12 770 GPa in the primary FCC phase to 96 864 GPa in the intermetallic μ, γ' phases. When the sintered samples were heat-treated at 700°C for five hours and air cooled the respective hardness is increased through a phenomenon called the annealing effect. The alloy $Fe_{20}Cr_{20}Mn_{20}Ni_{20}Ti_{10}Co_5V_5$ can retain its hardness and strength properties after annealing, up to an operating temperature of 700°C so it can be useful in high strength elevated temperature applications. The alloy exhibited a low coefficient of friction, wear resistance, and high densities compared to the other alloys sintered at 900°C and 870°C respectively. Future research on the alloy will include its application in high temperature and loaded engineering components and in corrosive environments. A further investigation of its crystal structure and how its changes with temperature is also required.

## References

Afolabi, A. E., Popoola, A. I. and Popoola, O. P. 2019. Spark Plasma Sintered High-Entropy Alloys: An Advanced Material for Aerospace Applications. In: Al-Naib, U. B., Vikraman, D. and Karuppasamy, K. eds. *Recent Advancements in the Metallurgical Engineering and Electrodeposition*. London: IntechOpen, 151-154.

Althahban, S., Pathinettampadian, G., Qahtani, F., Jazaa, Y., Mousa, S., Devi, S. A., De Poures, M. V., Subbiah, R. and Mamo, H. B. 2022. Process Optimization of Spark Plasma Sintering Parameters for Tungsten Carbide/Silicon Nitride/AA2219 Composites by Taguchi Method. Available: https://doi.org/10.1155/2022/4829499 (Accessed 15 October 2022).

Alvi, S. and Akhtar, F. 2019. High Temperature Tribology of Cumotawv High Entropy Alloy. *Wear*, 426: 412-419.

Bezold, A., Stone, H. J., Rae, C. M. F. and Neumeier, S. 2022. In Situ Investigation of TCP Phase Formation, Stress Relaxation and γ/γ' Lattice Misfit Evolution in Fourth Generation Single Crystal Ni-Base Superalloys by X-Ray High Temperature Diffraction. *Metallurgical and Materials Transactions*, 53(8): 2890-2901.

Bracq, G., Laurent-Brocq, M., Varvenne, C., Perrière, L., Curtin, W. A., Joubert, J. M. and Guillot, I. 2019. Combining Experiments and Modeling to Explore the Solid Solution Strengthening of High and Medium Entropy Alloys. *Acta Materialia*, 177: 266-279.

Burwell, J. T. and Strang, C. D. 1952. On the Empirical Law of Adhesive Wear. *Journal of Applied Physics*, 23(1): 18-28.

Chu, Q., Zhang, M., Li, J., Yan, F. and Yan, C. 2019. Nanoindentation Investigation of Ti/Fe Bimetallic Plate Welded by Vanadium Filler. *Metallurgical and Materials Transactions A*, 50: 2302-2309.

Chusong, E., Kansuwan, P., Ohtake, N., Wila, P., Tosangthum, N. and Tongsri, R. 2020. Dry-Sliding Wear of the 316l/H-Bn Composites Produced under Crack Ammonia Atmosphere. *Journal of Metals, Materials and Minerals*, 30(2): 117-123.

Cui, J., Cheng, Z., Chen, D., Wang, T., Zhang, L. and Sun, J. 2022. Studies on the Design and Properties of Fecrvtix Medium-Entropy Alloys for Potential Nuclear Applications. *Journal of Alloys and Compounds*, 894: 1-14.

Fischer-Cripps, A. C. 2010. *Nanoindentation (Mechanical Engineering Series)*. New York: Springer.

Ghasemi, S., Shanaghi, A. and Chu, P. K. 2017. Nano Mechanical and Wear Properties of Multi-Layer Ti/Tin Coatings Deposited on Al 7075 By High-Vacuum Magnetron Sputtering. *Thin Solid Films*, 638: 96-104.

Gohar, G. A., Manzoor, T. and Shah, A. N. 2018. Investigation of Thermal and Mechanical Properties of Cu-Al Alloys with Silver Addition Prepared by Powder Metallurgy. *Journal of Alloys and Compounds*, 735: 802-812.

Guruvidyathri, K., Hari Kumar, K. C., Yeh, J. W. and Murty, B. S. 2017. Topologically Close-Packed Phase Formation in High Entropy Alloys: A Review of Calphad and Experimental Results. *Jom*, 69: 2113-2124.

Haase, C. and Barrales-Mora, L. A. 2019. From High-Manganese Steels to Advanced High-Entropy Alloys. *Metals*, 9(7): 1-14.

He, Q. F., Ding, Z. Y., Ye, Y. F. and Yang, Y. 2017. Design of High-Entropy Alloy: A Perspective from Nonideal Mixing. *Jom*, 69: 2092-2098.

Helmut Fischer Technology Inc. 2022. Nanoindentation and most Important Parameters. Available: https://www.helmut-fischer.com/techniques/nanoindentation (Accessed 09 November 2022).

Horizon Technologies Inc. 2018. Powder Metal Material Properties: A Visual Flow of Possibilities. Available: https://www.horizontechnology.biz/Blog/Powder-Metal-Materials-Flow-Chart#:~:Text=Typically%2c%20the%20most%20common%20alloying,Properties%20in%20your%20structural%20application (Accessed 15 September 2022).

ISO14577. 2002. Metallic Materials–Instrumented Indentation Test for Hardness and Materials Parameters. Available: https://www.iso.org/standard/30104.html (Accessed 15 September 2022).

Jana, S., Sweet, L., Neal, D., Schemer-Kohrn, A., Lavender, C. and Joshi, V. 2018. The Role of Ternary Alloying Elements in Eutectoid Transformation of U10Mo Alloy Part I. Microstructure Evolution During Arc Melting and Subsequent Homogenization Annealing in U9. 8Mo0. 2X alloy (X= Cr, Ni, Co). *Journal of Nuclear Materials*, 509: 318-329.

Kang, J., Park, N., Kim, J. K. and Park, J. H. 2021. Role of Recrystallization and Second Phases on Mechanical Properties of (Cocrfemnni) 95.2 Al3. 2Ti1. 6 High Entropy Alloy. *Materials Science and Engineering*, 814: 1-11.

Kucharski, S. And Mróz, Z. 2011. Identification of Wear Process Parameters in Reciprocating Ball-on-Disc Tests. *Tribology International*, 44(2): 154-164.

Kushch, V. I., Dub, S. N. and Litvin, P. M. 2007. Determination of the Young Modulus from Elastic Section of the Berkovich Indenter Loading Curve. *Journal of Superhard Materials*, 29: 228-234.

Lee, S. H., Oh, H. C., An, B. H. and Kim, H. D. 2013. Ultra-Low Temperature Synthesis of Al4SiC4 Powder Using Spark Plasma Sintering. *Scripta Materialia*, 69(2): 135-138.

López Ríos, M., Socorro Perdomo, P. P., Voiculescu, I., Geanta, V., Crăciun, V., Boerasu, I. and Mirza Rosca, J. C. 2020. Effects of Nickel Content on the Microstructure, Microhardness and Corrosion Behavior Of High-Entropy Alcocrfenix Alloys. *Scientific Reports*, 10(1): 1-11.

Materials Today. 2022. Steel Annealing – Annealing Temperature, Stages, Types and Characterization. Available: https://www.nanoscience.com/Techniques/Nanoindentation/ (Accessed 24 August 2022).

Miracle, D. B. and Senkov, O. N. 2017. A Critical Review of High Entropy Alloys and Related Concepts. *Acta Materialia*, 122: 448-511.

Moreno, D., Kam, O., Wolfman, B., Nafman, O., Abrahami, S., Cohen, A., Nachmana, Y., Harush, Z. and Shapira, M. 2021. Titanium Carbide Effects on the Fracture of Inconel 100—A Case Study. *Journal of Minerals and Materials Characterization and Engineering*, 9(5): 432-443.

Murty, B. S., Yeh, J. W., Ranganathan, S. and Bhattachargee, S. S. 2019. *High Entropy Alloys*. 2nd Edition. Amsterdam: Elsevier.

Nano Science Instruments. 2022. Nanoindentation. Available: https://www.nanoscience.com/Techniques/Nanoindentation/ (Accessed 09 November 2022).

Nemecek, J. 2009. Nanoindentation of Heterogeneous Structural Materials. PhD Dissertation, Czech Technical University.

Ogunbiyi, O., Jamiru, T., Sadiku, R., Adesina, O., Lolu-Olajide, J. and Beneke, L. 2020. Optimization of Spark Plasma Sintering Parameters of Inconel 738LC Alloy Using Response Surface Methodology (RSM). *International Journal of Lightweight Materials and Manufacture*, 3(2): 177-188.

Oliver, W. C. and Pharr, G. M. 1992. An Improved Technique for Determining Hardness and Elastic Modulus Using Load and Displacement Sensing Indentation Experiments. *Journal of Materials Research*, 7: 1564–1583.

Oliver, W. C. and Pharr, G. M. 2004. Measurement of Hardness and Elastic Modulus by Instrumented Indentation: Advances in Understanding and Refinements to Methodology. *Journal of Materials Research*, 19(1): 3-20.

Onwuamaeze, I. P., Oyejide, J. O. and Salisu, S. 2018. The Effect of Annealing on the Microstructure and Mechanical Properties of Welded Carbon Steel. *Nigerian Research Journal of Engineering and Environmental Sciences*, 3(1): 96-102.

Qin, X. Z. and Yuan, Q. M. 2009. A Mu-Phase Behavior in a Cast Ni-Base Superalloy. *Journal of Materials Science*, 44(18): 4840-4847.

Rodriguez, A. A., Tylczak, J. H., Gao, M. C., Jablonski, P. D., Detrois, M., Ziomek-Moroz, M. and Hawk, J. A. 2018. Effect of Molybdenum on the Corrosion Behavior of High-Entropy Alloys CoCrFeNi 2 and CoCrFeNi 2 Mo 0.25 under Sodium Chloride Aqueous Conditions. *Advances in Materials Science and Engineering*, 2018: 1-12.

Schröders, S., Sandlöbes, S., Birke, C., Loeck, M., Peters, L., Tromas, C. and Korte-Kerzel, S. 2018. Room Temperature Deformation in the Fe7Mo6 μ-Phase. *International Journal of Plasticity*, 108: 125-143.

Sharma, N., Alam, S. N. and Ray, B. C. 2019. Fundamentals of Spark Plasma Sintering (SPS): An Ideal Processing Technique for Fabrication of Metal Matrix Nanocomposites. In: Cavaliere, P. ed. *Spark Plasma Sintering of Materials*. Switzerland: Cham: Springer, 21–59.

SKf Evolution. 2019. Wear and Surface Fatigue in Roller Bearings. Available: https://evolution.skf.com/Wear-And-Surface-Fatigue-In-Rolling-Bearings/ (Accessed 11 April 2013).

Sun, X., Li, L., Guo, Y., Zhao, H., Zhang, S., Yu, Y., Wu, D., Liu, H., Yu, M., Shi, D. and Liu, Z. 2018. Influences of Organic Component on Mechanical Property of Cortical Bone with Different Water Content by Nanoindentation. *AIP Advances*, 8(3): 1-10.

Tankiewicz, M. 2018. Application of the nanoindentation Technique for the Characterization of Varved Clay. *Open Geosciences*, 10(1): 902-910.

Tejedor, R., Rodríguez-Baracaldo, R., Benito, J. A., Cabrera, J. M. and Prado, J. M. 2008. Plastic Deformation of a Nanostructured and Ultra-Fine-Grained Fe-1% Cr with a Bimodal Grain Size Distribution. *International Journal of Material Forming*, 1: 487-490.

Total Materia. 2016. Spark Plasma Sintering. Available: https://www.totalmateria.com/page.aspx?ID=Home&LN=EN (Accessed 21 February 2022).

Tun, K. S., Gupta, M. and Srivatsan, T. S. 2020. Processing Challenges and Properties of Lightweight High Entropy Alloys. In: Srivatsan, T. S. and Gupta, M. eds. *High Entropy Alloys: Innovations, Advances, and Applications*. New York: CRC Press, 95–124.

Varvenne, C., Luque, A. and Curtin, W. A. 2016. Theory of Strengthening in Fcc High Entropy Alloys. *Acta Materialia*, 118: 64-176.

Xiao, J. K., Tan, H., Wu, Y. Q., Chen, J. and Zhang, C. 2020. Microstructure and Wear Behavior of Feconicrmn High Entropy Alloy Coating Deposited by Plasma Spraying. *Surface and Coatings Technology*, 385: 1-11.

Yang, L., Cheng, Z., Zhu, W., Zhao, C. and Ren, F. 2021. Significant Reduction in Friction and Wear of a High-Entropy Alloy Via the Formation of Self-Organized Nanolayered Structure. *Journal of Materials Science and Technology*, 73: 1-8.

Zhang, W., Zhang, X., Qiao, G., Zou, D., Zhou, Y. and Shen, C. 2019. Effect of Cobalt on the Microstructure and Corrosion Behavior of Martensitic Age-Hardened Stainless Steel. *Journal of Materials Engineering and Performance*, 28: 4197-4208.

Zhang, Y., Jiang, X., Sun, H. and Shao, Z. 2020. Effect of Annealing Heat Treatment on Microstructure and Mechanical Properties of Nonequiatomic Cocrfenimo Medium-Entropy Alloys Prepared by Hot Isostatic Pressing. *Nanotechnology Reviews*, 9(1): 580-595.

Zhao, Y., Li, L., Lu, Z., Teng, G., Liu, S., Hu, Z. and He, A. 2021. The Effect of Annealing Temperature on The Recrystallization and Mechanical Properties of Severe Plastic Deformed Commercial Pure Aluminium During Ultra-Fast Annealing. *Materials Research Express*, 8(4): 1-10.

Zhou, Y., Zhou, D., Jin, X., Zhang, L., Du, X. and Li, B. 2018. Design of Non-Equiatomic Medium-Entropy Alloys. *Scientific Reports*, 8(1): 1-9.

Zorzi, J. E. and Perottoni, C. A. 2013. Estimating Young's Modulus and Poisson's Ratio by Instrumented Indentation Test. *Materials Science and Engineering*, 574: 25-30.